Mathematics

https://www.aimspress.com/journal/Math

AIMS Mathematics, 11(8): 26720–26738.
DOI: 10.3934/math.20261072
Received: 29 April 2026
Revised: 03 August 2026
Accepted: 19 August2026
Published: 25 August2026

Research article

A data-driven ODE–PDE model for ramp impact on traffic flow on King Fahd Road in Riyadh

Yasser Almoteri and Abdulaziz Alsamil*

Department of Mathematics and Statistics, Imam Mohammad Ibn Saud Islamic University (IMSIU), Riyadh, Saudi Arabia

* **Correspondence:** Email: ASAlsamil@imamu.edu.sa.

Abstract: On-ramp inflows cause congestion on urban arterials. We present a coupled ODE–PDE model for traffic density on King Fahd Road, a 13 km corridor in Riyadh. The ODE represents diurnal ramp demand, calibrated from an independent feeder-road speed signal, and couples to the LWR conservation law via a localized source with a merge-admittance closure that limits injection by available supply. We introduce the ramp pressure number $R_p = L\alpha_0/(\rho_{\max} v_{\max}^2)$, a dimensionless control parameter, and non-dimensionalize the system. A conservative finite-volume method with characteristic-respecting boundary conditions solves the PDE; grid convergence and mass conservation confirm the numerics. Counterfactual simulations assess ramp metering, an extended acceleration lane, and merge capacity drop. Comparisons with independent mainline observations show the model captures the diurnal timing ($r = 0.88$) but under-predicts amplitude ($R^2 = 0.34$), which we attribute to the absence of a downstream bottleneck. The non-dimensional density stays within $[0, 1]$ and profiles show wave relaxation.

Keywords: traffic flow; LWR model; ramp demand; ODE-PDE coupling; finite volume; King Fahd Road; Riyadh
Mathematics Subject Classification: 35K57, 65M60, 65Z05, 92D25

1. Introduction

The rapid urban expansion of Riyadh has increased traffic congestion [1], with reports from 2025 placing average congestion at about 43.7% [2]. King Fahd Road, one of the primary arterial corridors connecting the northern and southern regions of the city, operates at nearly 300% of its intended daily vehicle capacity [3].

A major contributor to congestion on this corridor is the presence of on-ramps that inject vehicles into the main traffic stream. These localized inflows trigger nonlocal congestion effects, including backward-propagating shock waves that disrupt steady flow [4]. Quantifying the impact of ramp inflows is therefore necessary for effective traffic management and infrastructure planning.

Ramp metering (RM) has been the principal control response, and its methods have advanced steadily toward reducing congestion and raising throughput on urban freeways. Many studies evaluate RM effectiveness by comparing operational scenarios through detailed modelling and simulation [5–8]. The reported controllers include model predictive control (MPC) for coordinated operation across multiple bottlenecks [9, 10] and optimization- and learning-based schemes that stabilize mainline flow [11–13]. Destination-aware MPC manages off-ramp queues to prevent mainline disruption by optimizing vehicle assignment [9], constraint-aware controllers bound queue length under uncertain on-ramp demand [14], and combined strategies couple lane-change control with metering to distribute delay across the merge [15]. Empirical assessments report the effect of metering on safety and capacity [16] and on crash-related congestion using real-time data [17,18]. These strategies outperform basic feedback rules, but they refine the control input while leaving the physical dynamics of high-density merging unresolved, and they often rest on simplifying assumptions about queue spillover or on limited operational data.

A second strand develops computational frameworks for the flow mechanics themselves. Multi-scale models capture the interaction between ramp inflows and mainline traffic [19–21], and deep-learning and multi-agent methods sharpen traffic-state estimation [8,22]. Connected and autonomous vehicles (CAVs) introduce merging behaviours that require flow models for mixed autonomy [23–26]. Within continuum modelling, Chiarello [27] introduced source terms in nonlocal conservation laws for ramp dynamics, and Delle Monache et al. [28] proposed a coupled PDE–ODE model in which the ODE governs queue dynamics at a ramp buffer; our formulation instead lets the ODE govern the temporal demand amplitude feeding a distributed source, rather than a point buffer at a junction. Kolb et al. [29] used second-order models to reproduce capacity-drop phenomena and evaluate metering; we retain a first-order scalar description for its well-posed structure and transparent dimensionless scaling, and represent the merge capacity drop through a local capacity factor rather than a second-order momentum equation (Section 5.6). Related studies span microscopic ramp behaviour reproduced through macroscopic flow [30], macroscopic models of ramp effects during peak periods [31], microscopic simulation of mixed traffic at on-ramp bottlenecks [32], and data-driven analysis of ramp inflow [33]. Several of these efforts move toward LWR-based solvers and reinforcement learning [13,22].

Despite mature RM optimization and capable flow solvers for CAV and mixed-autonomy settings, no single model quantifies localized physical failure from merging stress under real-world temporal variability. Existing work simplifies either the coupling between mainline flow and diurnal ramp demand or the mechanical bottleneck at the merge zone. Steady-state performance indicators such as the volume-to-capacity (v/c) ratio and bottleneck-strength measures are well established [34], but they characterize a link's aggregate loading rather than the localized, time-varying forcing a ramp exerts on the evolving density field. Capturing the coupling between external, macro-scale demand and local congestion dynamics requires a framework beyond the optimization of control inputs.

The present work addresses this gap with a coupled ODE–PDE framework that links a multi-harmonic model of diurnal ramp demand (the ODE) to the Lighthill–Whitham–Richards (LWR) conservation law (the PDE) through a merge-admittance source term representing the physical limit on injection at the merge point. The demand signal is taken from an independent feeder-road measurement rather than the mainline state, which avoids driving the model with the quantity it predicts, and the predicted mainline density is then checked against independent mainline observations. Ramp forcing is condensed into a single dimensionless control parameter R_p within a complete non-dimensionalization, and the scalar law is solved with conservative, grid-convergent finite-volume schemes under well-posed boundary conditions. The contributions are: (i) the ramp pressure number and a dimensionally consistent non-dimensional formulation; (ii) a merge-admittance source closure that keeps the density within physical bounds; (iii) a conservative, grid-convergent finite-volume solution with well-posed boundary conditions; (iv) quantitative policy counterfactuals; and (v) an independent mainline validation, reported with its limitations. Together these quantify merge friction as the dominant lever near capacity, a regime that remains poorly constrained.

2. Mathematical model

2.1. Road geometry and modeling assumptions

We consider the north–south section of King Fahd Road in Riyadh, from the Northern Ring Road interchange ($x = 0$) to the Makkah Road interchange ($x = L$), with total length $L = 13$ km. Traffic is modeled as a one-dimensional macroscopic system along the main-road centerline. A major on-ramp lies over $[x_1, x_2] = [4.1, 4.3]$ km.

The following assumptions are adopted:

- traffic flow is approximated as one-dimensional;
- vehicle density is an averaged macroscopic quantity;
- ramp inflow acts as a localized source subject to a supply (admittance) constraint;
- lane-changing and weaving friction near the merge are represented aggregately by a local capacity factor $c(x) \leq 1$ (Section 2.4), rather than resolved microscopically.

2.2. Ramp demand ODE model

Let $D(t)$ denote the time-dependent ramp demand. We model it by the first-order linear ODE

$$\frac{dD}{dt} = f(t) - \delta D(t), \qquad t \in (0, T], \tag{2.1}$$

where $\delta > 0$ is the demand relaxation rate and $f(t)$ is a periodic forcing. To capture the morning and the sharper afternoon peak, we represent f by a multi-harmonic Fourier series

$$f(t) = a_0 + \sum_{k=1}^{K} \left[a_k \sin(k\omega t) + b_k \cos(k\omega t)\right], \qquad \omega = \frac{2\pi}{24}, \tag{2.2}$$

with ω corresponding to a 24-hour cycle. The coefficients are estimated by least squares (Section 3); a single harmonic ($K = 1$) produces one broad peak, whereas $K \geq 2$ resolves the two distinct daily peaks. The initial condition is $D(0) = D_0$, taken from the fitted demand.

2.3. Main road traffic PDE model

Let $\rho(x, t)$ denote traffic density (veh/km) at $x \in (0, L)$, $t \in (0, T]$. The dynamics obey the LWR conservation law

$$\frac{\partial \rho}{\partial t} + \frac{\partial}{\partial x} q(\rho) = s(x, t), \quad x \in (0, L),\ t \in (0, T], \tag{2.3}$$

with the Greenshields flux, generalized by a local capacity factor $c(x) \in (0, 1]$ that encodes merge friction,

$$q(\rho; x) = c(x)\, v_{\max}\, \rho \left(1 - \frac{\rho}{\rho_{\max}}\right), \tag{2.4}$$

where $v_{\max}$ is the free-flow speed and $\rho_{\max}$ the jam density; $c(x) = 1$ away from the merge.

2.4. ODE–PDE coupling and the merge-admittance closure

The coupling is a localized source $s(x, t) = \alpha(x)D(t)$, where $\alpha(x)$ describes the ramp's spatial influence over $[x_1, x_2]$ with intensity $\alpha_0 > 0$. A purely additive source is, however, unphysical near jam density: Because the dimensionless demand $\tilde{D} = v_{\max}D$ is $O(10)$ for realistic travel times, an unconditioned source drives ρ past $\rho_{\max}$. The physical resolution is that a ramp cannot inject vehicles into road that is already at jam density: The admitted inflow is limited by the available downstream supply, proportional to $(\rho_{\max} - \rho)$. This yields the merge-admittance closure

$$s(x, t) = \alpha(x)\, D(t) \left(1 - \frac{\rho}{\rho_{\max}}\right)_+, \qquad (\,\cdot\,)_+ = \max(\,\cdot\,, 0), \tag{2.5}$$

so that injection vanishes as $\rho \to \rho_{\max}$ and ρ never exceeds jam density. For $\rho \ll \rho_{\max}$ (free flow) the factor $\to 1$ and (2.5) reduces to the classical additive source $\alpha(x)D(t)$; the closure is thus a supply-limited generalization that acts only near capacity, in the spirit of merge and cell-transmission models. For King Fahd Road the ramp region is $[x_1, x_2] = [4.1, 4.3]$ km; the source extends verbatim to multiple ramps as $s(x, t) = \sum_i \alpha_i(x)D_i(t)\,(1 - \rho/\rho_{\max})_+$.

2.5. Initial and boundary conditions

The initial density is $\rho(x, 0) = \rho_0(x)$, $0 \le x \le L$, set to the baseline arterial state. Boundary conditions are imposed through ghost cells:

- **Inflow** ($x = 0$)**:** A prescribed, realistic, non-zero density $\rho(0, t) = \rho_{in}(t)$. On the free-flow branch ($\rho < \rho_{\max}/2$) the characteristic enters the domain from the left, so prescribing the inflow state is well posed. A mild diurnal $\rho_{in}(t)$ makes the corridor busy but uncongested even without ramp injection.
- **Outflow** ($x = L$)**:** A transmissive (zero-gradient) condition, realized by copying the last interior cell into the outflow ghost cell. This is characteristic-respecting for outgoing waves and produces no reflection.

A fixed (Dirichlet) density is not imposed at the outflow, which would be ill-posed for outgoing characteristics and would seed spurious downstream reflections.

2.6. Dimensionless formulation

Introduce

$$\tilde{x} = \frac{x}{L}, \quad \tilde{t} = \frac{t}{\tau}, \quad \tilde{\rho} = \frac{\rho}{\rho_{\max}}, \quad \tau = \frac{L}{v_{\max}}, \quad \tilde{D} = v_{\max}D.$$

Substituting into (2.3)–(2.5) with $c \equiv 1$, the time term scales as $\rho_{\max}/\tau$ and the flux term as $v_{\max}\rho_{\max}/L$; dividing through by $v_{\max}\rho_{\max}/L$ and using $\tau = L/v_{\max}$ makes both coefficients unity, leaving the source coefficient $L\alpha_0/(\rho_{\max}v_{\max})$ multiplying $\bar{\alpha}(\tilde{x})D$. Writing $D = \tilde{D}/v_{\max}$ collects this into the single group

$$R_p = \frac{L\alpha_0}{\rho_{\max}v_{\max}^2}. \tag{2.6}$$

Dropping tildes, the non-dimensional coupled system is

$$\frac{\partial\rho}{\partial t} + \frac{\partial}{\partial x}\left[\rho(1-\rho)\right] = R_p\,\bar{\alpha}(x)\,d(t)\,(1-\rho)_+, \tag{2.7}$$

$$\frac{dD}{dt} = f(t) - \delta D(t), \tag{2.8}$$

where $\bar{\alpha}$ is a unit-peak shape over $[\tilde{x}_1, \tilde{x}_2]$ and $d(t) = \tilde{D}(t)/\max_t \tilde{D}(t) \in [0, 1]$ is the demand's diurnal profile (peak 1). With this normalization R_p is the peak dimensionless injection rate into a free road, swept as the control parameter. Unlike the volume-to-capacity (v/c) ratio, which evaluates the steady-state loading of a link, R_p is a dynamic source-term scaling parameter: It quantifies the localized, time-varying spatial forcing of a ramp relative to mainline wave propagation, and enters the governing conservation law directly rather than summarizing an aggregate demand level.

Dimensional consistency of R_p. Table 1 lists the base dimensions (units: veh, km, h). The source $[s] = [\alpha_0][D] = \mathrm{veh\,h^{-2}} \cdot \mathrm{h\,km^{-1}} = \mathrm{veh\,km^{-1}h^{-1}}$ is a density rate, and

$$[R_p] = \frac{[L][\alpha_0]}{[\rho_{\max}][v_{\max}]^2} = \frac{\mathrm{km}\cdot\mathrm{veh\,h^{-2}}}{\mathrm{veh\,km^{-1}}\cdot\mathrm{km^2h^{-2}}} = 1,$$

so R_p is dimensionless. The admittance factor $(1-\rho/\rho_{\max})$ and the profile $d(t)$ are dimensionless, hence the closure does not affect this result.

Table 1. Base dimensions used in the non-dimensionalization (Section 2.6).

Symbol	Meaning	Dimension
L	corridor length	km
$v_{\max}$	free-flow speed	$\mathrm{km\,h^{-1}}$
$\rho, \rho_{\max}$	density, jam density	$\mathrm{veh\,km^{-1}}$
D	ramp demand signal	$\mathrm{h\,km^{-1}}$
α_0	ramp influence amplitude	$\mathrm{veh\,h^{-2}}$
τ	time scale $L/v_{\max}$	h
R_p	ramp pressure number	1 (dimensionless)

2.7. Well-posedness of the coupled system

Equation (2.1) is a linear ODE with continuous forcing; by the Picard–Lindelöf theorem it has a unique global solution. Equation (2.3) is a scalar hyperbolic conservation law with a Lipschitz flux and a bounded source that vanishes as $\rho \to \rho_{\max}$; with the well-posed inflow data of Section 2.5 it admits a unique entropy solution. Because the source is localized and bounded and the admittance factor keeps $\rho \in [0, 1]$, the coupled system is well posed and suitable for numerical simulation.

3. Data and calibration

3.1. Automated data collection

Hourly traffic data were collected automatically over five consecutive weekdays using a custom Python script interfaced with the mapbox directions API. The script queries traffic-aware driving directions exactly on the hour (Riyadh local time, UTC+3) for two independent segments: (i) a 1.8 km feeder-road segment whose inverse speed $D(t) = 1/v_{\text{feeder}}(t)$ supplies the ramp-demand signal, and (ii) a short mainline segment at $x = 8$ km used for downstream validation. Speeds, timestamps, and day-of-week labels are appended incrementally to CSV files.

3.2. Corridor speed scale and the independent demand signal

The free-flow speed scale is derived from observed corridor travel times rather than assumed. Table 2 lists 24-hour travel times for the corridor; their minimum (fastest) trip is 12 minutes, which sets

$$v_{\max} = \frac{L}{\min_h T(h)} = \frac{13\,\text{km}}{0.2\,\text{h}} = 65\,\text{km/h}, \qquad \tau = \frac{L}{v_{\max}} = 0.2\,\text{h} = 12\,\text{min}.$$

These travel times fix the free-flow speed scale only; the ramp demand is supplied by the independent feeder signal described below.

Table 2. Observed 24-hour corridor travel times used to derive the free-flow speed scale $v_{\max} = 65$ km/h from the fastest (12 min) trip.

Time	08:00	09:00	10:00	11:00	12:00	13:00	14:00	15:00	16:00	17:00	18:00	19:00
Travel (min)	18	18	19	19	18	18	19	25.5	32.5	39.5	40.5	30
Time	20:00	21:00	22:00	23:00	00:00	01:00	02:00	03:00	04:00	05:00	06:00	07:00
Travel (min)	22	20	18	18	16	13	13	13	12	12	13	15

The ramp demand is driven by an independent signal: the on-ramp feeder-road speed, which is not the mainline quantity the PDE predicts. Using the mainline speed itself to define the demand would create a circular dependence, since mainline speed is a response to density; the feeder approach avoids this. The demand is the feeder inverse speed

$$D(t) = \frac{1}{v_{\text{feeder}}(t)} = \frac{T_{\text{feeder}}(t)}{L_{\text{feeder}}} \quad [\text{h}\,\text{km}^{-1}], \tag{3.1}$$

independent of mainline congestion. The calibration uses hourly feeder speeds over five consecutive weekdays (Riyadh local time), with full 0–23 h coverage on each day, over a feeder segment $L_{\text{feeder}} =$ 1.8 km. The feeder speed drops from $\approx$ 60 km/h overnight to $\approx$ 15 km/h at the afternoon peak (a factor of $\approx$ 4), a strong, non-flat diurnal signal. Keeping the five days separate permits confidence intervals on the fitted coefficients (Section 3.4).

3.3. Parameter values

Table 3 lists the physical and numerical parameters with their values, units, and provenance.

Table 3. Physical and numerical parameters.

Symbol	Value	Unit	Source / note
L	13	km	corridor length, measured
x_1, x_2	$4.1, 4.3$	km	on-ramp merge zone
$\rho_{\max}$	150	veh/km/lane	per-lane jam density ($\approx$ 6.7 m/veh); see below
$v_{\max}$	65	km/h	derived: $L/\min_h T(h)$
τ	0.2	h	derived: $L/v_{\max}$
δ	0.30	h^{-1}	demand relaxation rate
ω	$2\pi/24$	rad/h	diurnal frequency
α_0	9750	veh/h^2	ramp amplitude (at $R_{p,\mathrm{ref}} = 0.2$)
R_p	0–1	–	control parameter (dimensionless)
ρ_{in}	0.28–0.43	–	diurnal inflow density (non-dim)
N_x	200	–	finite-volume cells
C_{CFL}	0.45	–	CFL number
T	24	h	simulated horizon

The jam density is taken on a per-lane basis: $\rho_{\max} = 150$ veh/km/lane ($\approx$ 6.7 m/vehicle). The corridor is modeled as an aggregated single-lane macroscopic link, the standard one-dimensional LWR simplification; this preserves the dimensional scaling, the derived $v_{\max}$, and the definition of R_p. A sensitivity range of $[120, 180]$ veh/km/lane bounds the effect of this choice.

3.4. Multi-harmonic fit, goodness of fit, and parameter uncertainty

The forcing (2.2) is fitted to the feeder signal for $K = 1, 2, 3$. Table 4 reports R^2, RMSE, and MAE. A single harmonic ($K = 1$, $R^2 = 0.44$) captures only one broad peak; $K \geq 2$ resolves the separate morning and afternoon peaks, and $K = 3$ ($R^2 = 0.94$) sharpens the afternoon peak (Figure 2).

Table 4. Fourier fit metrics for the independent feeder demand signal.

Signal	K	R^2	RMSE	MAE
feeder (independent)	1	0.441	0.0110	0.0088
	2	0.738	0.0075	0.0065
	3	0.939	0.0036	0.0029

Because the five weekdays are kept separate, we fit the $K = 3$ model to each day and report each coefficient's mean and 95% confidence interval from the across-day scatter ($n = 5$; Table 5). The intervals are narrow, indicating a stable diurnal signal across the observed week. The relaxation rate $\delta = 0.30$ h^{-1} is a fixed modeling choice, so no interval is reported for it.

Table 5. Fitted Fourier coefficients ($K = 3$) with 95% confidence intervals from the across-day scatter of the five weekdays. Units: $\mathrm{h\,km^{-1}}$.

Coefficient	Mean	95% CI low	95% CI high
a_0	0.0316	0.0301	0.0331
a_1	−0.0092	−0.0105	−0.0079
b_1	−0.0103	−0.0112	−0.0093
a_2	−0.0007	−0.0009	−0.0005
b_2	−0.0113	−0.0128	−0.0097
a_3	0.0051	0.0047	0.0056
b_3	0.0078	0.0067	0.0088

4. Numerical method

4.1. Finite-volume discretization and boundary conditions

The domain $[0, 1]$ is divided into N_x uniform cells of width $\Delta x = 1/N_x$. With cell averages ρ_j^n, the conservative update is

$$\rho_j^{n+1} = \rho_j^n - \frac{\Delta t}{\Delta x}\left(F^n_{j+\frac{1}{2}} - F^n_{j-\frac{1}{2}}\right) + \Delta t\, s_j^n, \tag{4.1}$$

where $s_j^n = R_p\, \bar{\alpha}_j\, d(t_n)\,(1 - \rho_j^n)_+$. Boundary conditions are applied through ghost cells (Section 2.5): The left ghost holds the prescribed inflow density and the right ghost copies the last interior cell (transmissive outflow). Summing (4.1) over j telescopes the fluxes, so the scheme conserves mass exactly up to the boundary fluxes and the source (Section 4.5).

4.2. First- and second-order fluxes

The first-order scheme uses the Rusanov (local Lax–Friedrichs) flux

$$F^n_{j+\frac{1}{2}} = \tfrac{1}{2}\Big[q(\rho_j^n) + q(\rho_{j+1}^n)\Big] - \tfrac{1}{2}\, a^n_{j+\frac{1}{2}}\Big(\rho^n_{j+1} - \rho^n_j\Big), \quad a^n_{j+\frac{1}{2}} = \max\Big(|q'(\rho_j^n)|, |q'(\rho_{j+1}^n)|\Big). \tag{4.2}$$

Because first-order Rusanov is diffusive, we also employ a second-order high-resolution scheme: MUSCL reconstruction with a minmod limiter and a two-stage strong-stability-preserving Runge–Kutta (SSP-RK2) time integrator. The merge capacity factor $c(x)$ enters through face-averaged values in (4.2).

4.3. Coupling and CFL condition

At each step the demand ODE (2.1) is advanced, the bounded source s_j^n is evaluated, interface fluxes are computed, the density is updated by (4.1), and the ghost-cell boundary conditions are applied. The time step obeys the CFL condition

$$\Delta t \le C_{\mathrm{CFL}}\, \frac{\Delta x}{\max |q'(\rho)|}, \qquad C_{\mathrm{CFL}} = 0.45, \tag{4.3}$$

enforced adaptively each step.

4.4. Grid convergence

Grid convergence is quantified by self-convergence against a fine ($N_x = 1600$) reference for the coupled problem at $R_p = 1$, restricting the reference to each coarse grid by exact cell-averaging. Table 6 reports L_1, L_2, L_∞ errors and the observed order over $N_x = 100$–800. The first-order scheme converges at first order (with super-first-order behavior where the solution is smooth), while the second-order scheme attains second order with errors roughly an order of magnitude smaller. The formal first order of the Rusanov scheme is confirmed separately against the exact scalar Riemann solution for shock and rarefaction data.

Table 6. Grid-convergence study for the coupled problem ($R_p = 1$).

Scheme	N_x	L_1	L_2	L_∞	ord. L_1	ord. L_2	ord. L_∞
Rusanov	100	2.74×10^{-4}	4.08×10^{-4}	2.47×10^{-3}	–	–	–
	200	3.68×10^{-5}	1.40×10^{-4}	1.23×10^{-3}	2.90	1.54	1.00
	400	1.40×10^{-5}	5.89×10^{-5}	5.22×10^{-4}	1.39	1.25	1.24
	800	4.67×10^{-6}	1.96×10^{-5}	1.74×10^{-4}	1.59	1.59	1.59
MUSCL	100	2.51×10^{-4}	3.60×10^{-4}	2.23×10^{-3}	–	–	–
	200	1.45×10^{-5}	5.24×10^{-5}	5.21×10^{-4}	4.12	2.78	2.10
	400	2.19×10^{-6}	1.14×10^{-5}	1.15×10^{-4}	2.73	2.20	2.17
	800	4.70×10^{-7}	2.47×10^{-6}	2.61×10^{-5}	2.22	2.20	2.15

At the merge front (Figure 1) the second-order scheme resolves an about 1.14× steeper front and a 10–90% rise width of 0.13 km versus 0.20 km, with an L_1 error against the reference about 4.3× smaller than the first-order scheme, quantifying the latter's numerical diffusion.

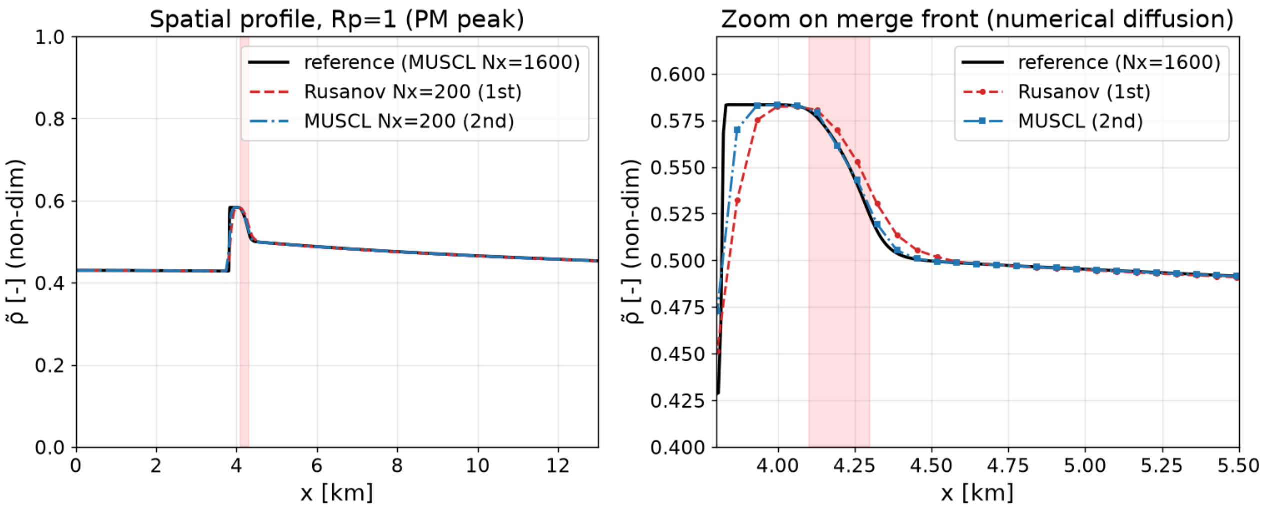

Figure 1. First-order Rusanov vs. second-order MUSCL at the merge front ($R_p = 1$, $N_x = 200$) against a fine reference. Right: Zoom showing the numerical diffusion of the first-order scheme. All densities are non-dimensional and within $[0, 1]$.

4.5. Mass conservation

The discrete global mass balance $M(t) - M(0) - [\text{influx} - \text{outflux} + \text{source}]$ remains at machine precision ($\leq 2.3 \times 10^{-13}$) over the full 24 h for every $R_p \in [0, 1]$. Because the merge-admittance closure keeps $\rho \leq 1$ by construction, no boundedness projection onto $[0, 1]$ is ever activated: No vehicles are artificially added or removed. The global maximum density over the sweep is $\rho \simeq 0.583$.

4.6. Discretization parameters

For the reported runs, $N_x = 200$, giving $\Delta x = 0.005$ (non-dimensional) $= 0.065$ km; the adaptive time step at $C_{\text{CFL}} = 0.45$ produces about 1.5×10^4 steps over the 24 h horizon.

5. Results and discussion

5.1. Ramp demand calibration

Figure 2 compares the independent feeder demand signal with the multi-harmonic Fourier fits. The single-harmonic fit ($K = 1$, $R^2 = 0.44$) captures only one broad peak, whereas $K = 3$ ($R^2 = 0.94$) resolves the morning and the sharper afternoon peaks, with the fitted-parameter confidence intervals of Table 5.

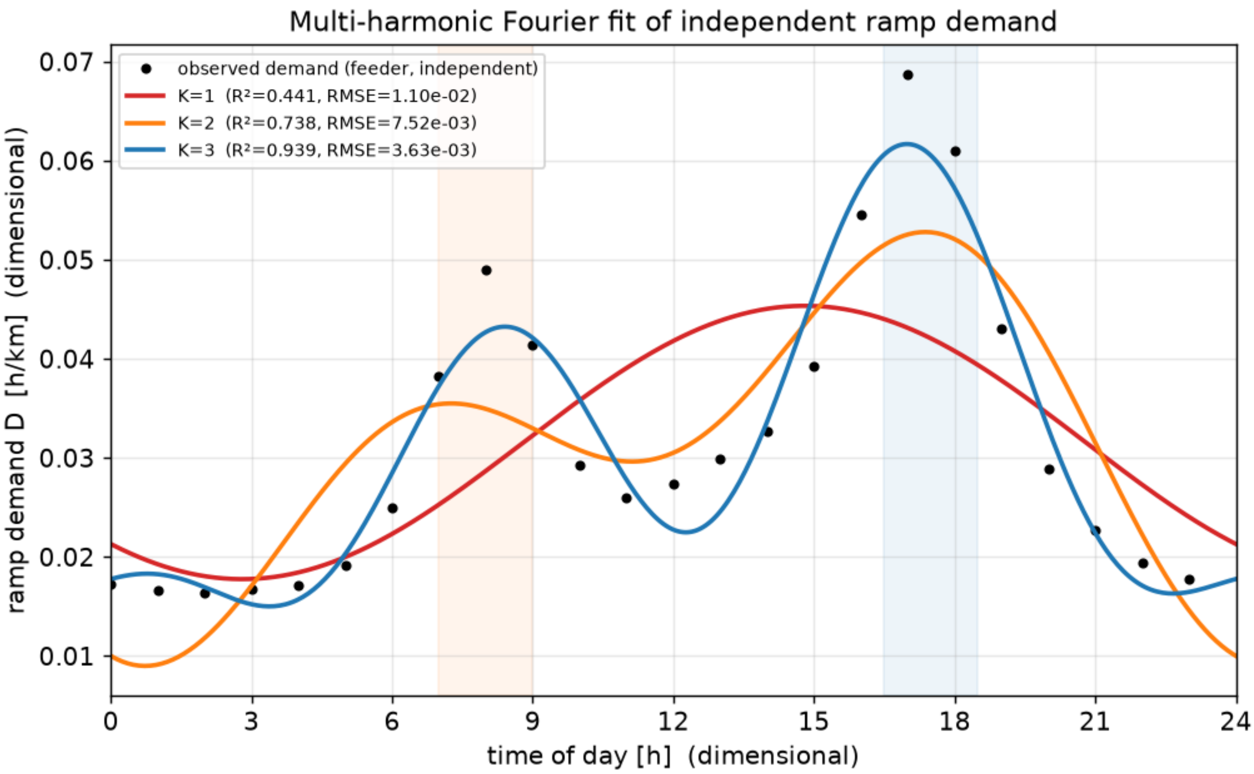

Figure 2. Multi-harmonic Fourier fit of the independent feeder ramp-demand signal ($K = 1, 2, 3$; five weekdays). Axes are dimensional (time in h, demand in h/km).

5.2. Validation against independent mainline observations

We compare the predicted mainline density against independent mainline observations: Hourly mainline speeds over five weekdays at a fixed downstream station $x = 8$ km (well past the merge), a measurement distinct from the feeder demand signal. Observed speeds are converted to density through the Greenshields relation $\tilde{\rho} = 1 - v/v_{\max}$. The model is run at its documented operating point (feeder-calibrated demand, $R_p = 1$, default diurnal inflow), fixed independently of the validation record; predicted density is extracted at the same location and hours.

The agreement is fair (Figure 3a). The model reproduces the diurnal structure the morning (~08:00) and afternoon (~17:00) congestion peaks and the overnight recovery, with a temporal correlation $r =$ 0.88 but under-predicts the amplitude: the observed density swings from $\tilde{\rho} \approx 0.05$ overnight to ≈ 0.76 at the afternoon peak, whereas the model spans only $\approx$ 0.32–0.49 ($R^2 = 0.34$, RMSE = 0.19, mean bias ≈ 0). Two model choices account for the amplitude gap: the illustrative "busy" baseline inflow ($\tilde{\rho}_{\text{in}} \approx 0.28$) over-estimates the near-empty observed overnight state ($\tilde{\rho} \approx 0.07$), and a single downstream station cannot constrain the upstream boundary. The model therefore captures the timing and phase of congestion but not its full magnitude.

Attribution of the amplitude gap. To localize the cause, Figure 3(b) re-runs the model with only the upstream inflow constants (baseline level and amplitude) fit to the mainline observations, everything else unchanged. This is a boundary calibration used purely as a diagnostic; the inflow is fit to the same record being compared, so it is not an independent validation and is not interpreted as one. It shows that part of the gap is attributable to the uncalibrated upstream boundary (calibrating the inflow raises R^2 from 0.34 to 0.46 and matches the observed overnight low state) but does not close it. The reason is structural: The observed afternoon density ($\tilde{\rho} \approx 0.76$) lies on the congested branch ($\tilde{\rho} > 1/2$), whereas the transmissive downstream boundary lets waves exit freely and keeps $x = 8$ km on the free-flow branch. Without a modeled downstream bottleneck to back congestion up to the station, the scheme cannot reach a congested-branch density there regardless of the inflow. The gap is thus a boundary-condition effect (the upstream inflow level and a missing downstream constraint) rather than a failure of the interior dynamics, and points to a downstream boundary/bottleneck condition (Section 7) as the concrete next step.

5.3. Temporal evolution of traffic density

Figure 4 shows the density at a downstream point ($x = 8$ km) over 24 h for $R_p \in \{0, 0.2, 0.4, 0.6, 0.8, 1\}$. At $R_p = 0$ the corridor is busy but uncongested ($\tilde{\rho} \in [0.32, 0.43]$), not near zero, reflecting the realistic diurnal inflow. As R_p increases, the density peaks grow and follow the demand pattern; near $R_p = 1$ the afternoon peak crosses the capacity level $\tilde{\rho} = 0.5$. All values remain within $[0, 1]$.

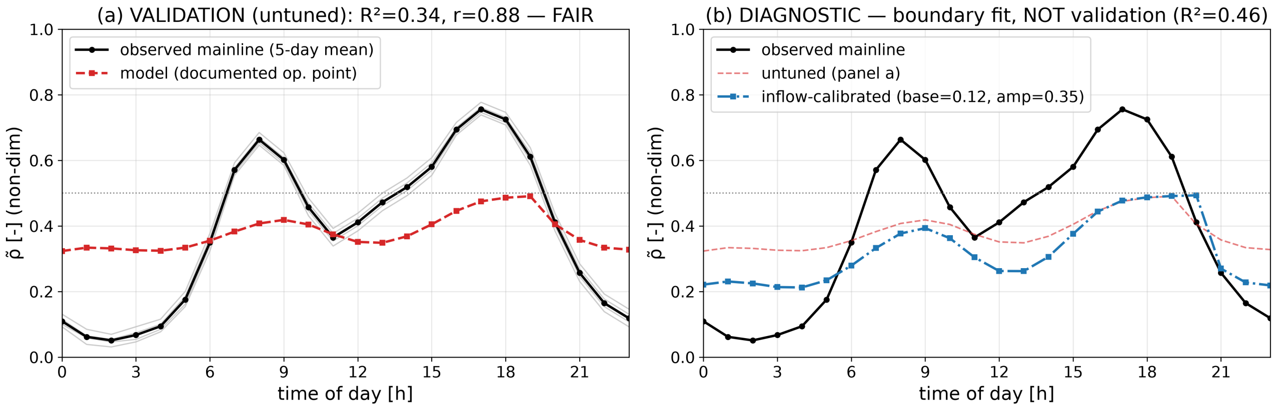

Figure 3. (a) Validation at $x = 8$ km: observed mainline density (5-weekday mean, individual days in grey) vs. the model at its documented operating point, with no parameter fit to the observations; the model captures the diurnal timing ($r = 0.88$) but under-predicts the amplitude ($R^2 = 0.34$). (b) Diagnostic (boundary calibration, not an independent validation): fitting only the upstream inflow constants to the same observations raises R^2 to 0.46 but cannot close the amplitude gap, isolating it as a boundary-condition effect. All densities are non-dimensional.

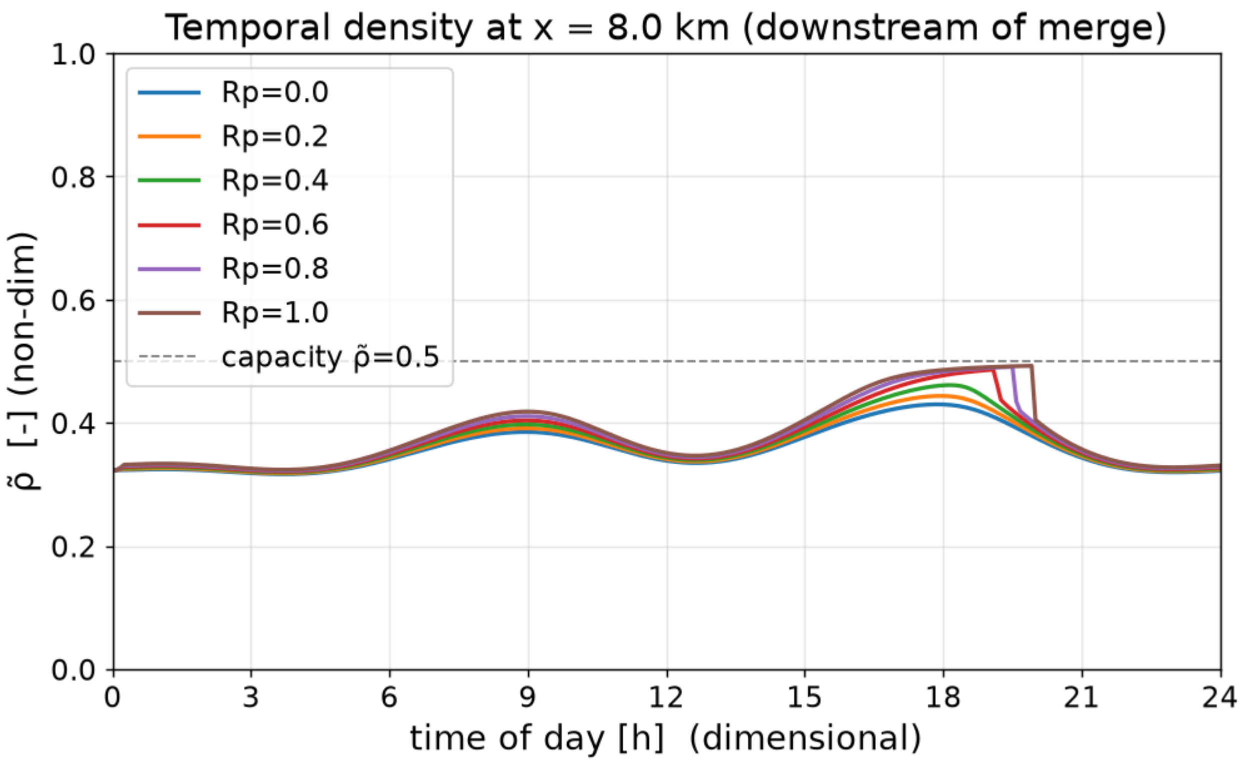

Figure 4. Temporal density at $x = 8$ km for varying R_p. The vertical axis is the non-dimensional density $\tilde{\rho} \in [0, 1]$; the dashed line marks capacity $\tilde{\rho} = 0.5$.

5.4. Spatial profiles and downstream wave structure

Figure 5 shows spatial density profiles at the afternoon peak. A localized rise at the merge is followed by a smooth downstream relaxation gradient, i.e., genuine characteristic wave structure, and there is no spurious feature at the outflow $x = 13$ km. At higher R_p and with a merge capacity drop, an upstream queue forms with a downstream rarefaction, the classic bottleneck signature.

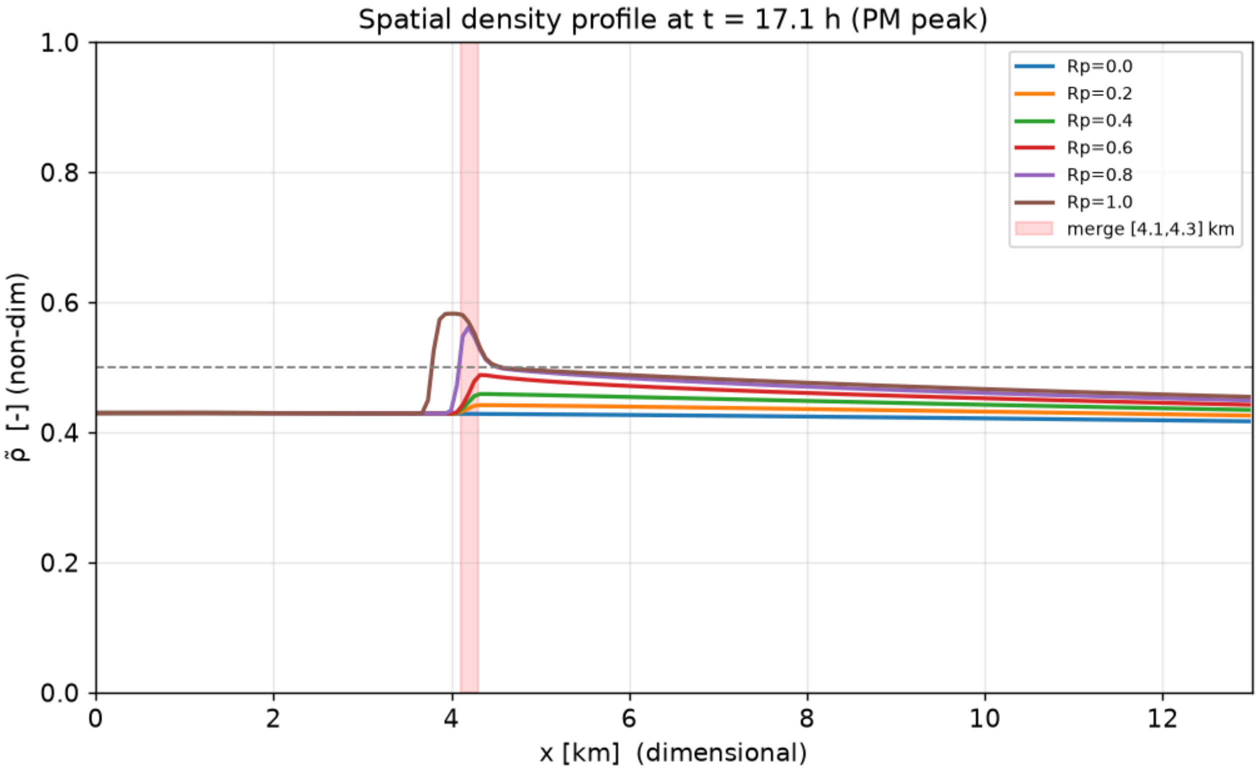

Figure 5. Spatial density profiles at the afternoon peak for varying R_p. The shaded band marks the merge $[4.1, 4.3]$ km; the horizontal axis is dimensional (x in km) and the vertical axis is $\tilde{\rho} \in [0, 1]$.

5.5. Physical interpretation of the ramp pressure number

R_p is the dimensionless amplitude of the ramp forcing relative to mainline throughput: Small R_p perturbations are absorbed by the stream, while larger R_p pushes the merge toward and past capacity. Because R_p enters the source directly, it provides a single tunable knob for policy analysis (Section 6).

5.6. Model choice and lane-changing

We adopt first-order LWR for its well-posed scalar structure, its transparent dimensionless scaling through R_p, and its mass-exact finite-volume treatment. First-order models cannot represent non-equilibrium phenomena (capacity drop, driver reaction delays, and phase transitions) that second-order continuum models (Payne–Whitham, Aw–Rascle–Zhang) capture. Rather than adopt a full second-order model, we emulate the dominant merge effect, the capacity drop induced by lane-changing and weaving, through the local capacity factor $c(x) \leq 1$ in (2.4). Section 6 quantifies its impact; a full ARZ/PW treatment is a natural extension.

6. Policy scenarios

We evaluate three counterfactuals over 24 h. The baseline is the uncontrolled ramp at $R_p = 1$ with a modest merge capacity drop ($c = 0.95$ over the merge, representing the empirically-documented capacity-drop phenomenon; the value is illustrative): Real on-ramp merges lose capacity to lane-changing and weaving, so a realistic baseline includes this drop. The interventions act on the two available levers, ramp demand R_p and merge capacity c:

- **Ramp metering:** Cap the ramp pressure at $R_p \leq 0.4$;
- **Acceleration lane:** An extended acceleration lane lets merging vehicles reach mainline speed, removing the merge capacity drop ($c \to 1$), with ramp demand unchanged;
- **Merge capacity drop (sensitivity):** A heavier, unmitigated drop ($c = 0.80$) representing severe lane-changing friction.

We report the change versus baseline in three metrics: Peak density; the congestion duration (hours the spatial maximum exceeds capacity $\tilde{\rho} = 0.5$); and a delay proxy equal to the non-dimensional Greenshields extra-travel-time integral $\iint \tilde{\rho}^2/(1 - \tilde{\rho})\, d\tilde{x}\, d\tilde{t}$ (the density form of $\rho\,(1/v(\rho) - 1/v_{\max})$). Results are in Table 7 and Figure 6.

Table 7. Scenario metrics vs. baseline (peak $\tilde{\rho} = 0.619$, congestion 7.83 h, delay proxy 30.80). These are model outputs; the reported congestion reductions are simulated, not field-measured.

Scenario	Δ peak density	Δ congestion dur.	Δ delay proxy
Baseline (R_p=1, c=0.95)	—	—	—
Ramp metering ($R_p \leq 0.4$)	−1.8%	−27.7%	−7.3%
Acceleration lane ($c \to 1$)	−5.9%	−58.5%	−8.4%
Merge capacity drop (c=0.80)	+14.5%	+205.9%	+132.1%

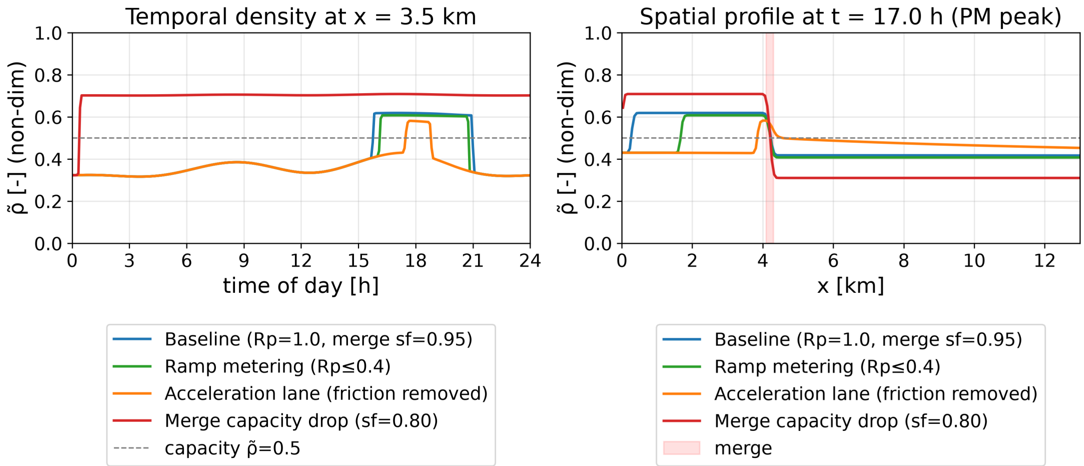

Figure 6. Scenario comparison. Left: Temporal density just upstream of the merge ($x = 3.5$ km), where the bottleneck queue forms. Right: Spatial profile at the afternoon peak, showing the upstream queue and downstream rarefaction for the capacity-drop case. All densities are non-dimensional and within [0, 1].

Near a capacity-limited merge, merge friction dominates ramp demand: An acceleration lane that removes the capacity drop produces the largest reduction in congestion duration, ramp metering yields a smaller improvement, and unaddressed lane-changing friction sharply increases total delay (more than doubling it here). These percentages are simulated model outputs; the transferable conclusion is the sign and ordering of the interventions, which are stable, rather than the precise magnitudes.

7. Conclusions

We developed a coupled ODE–PDE framework for ramp-induced congestion on King Fahd Road. A multi-harmonic demand ODE, driven by an independent feeder signal, is coupled to the LWR PDE through a merge-admittance source that keeps the non-dimensional density within [0, 1] without any bounded-projection step. The ramp pressure number $R_p = L\alpha_0/(\rho_{\max} v_{\max}^2)$ is dimensionless and serves as the single control parameter. The scalar PDE is solved with ghost-cell boundary conditions (realistic inflow, transmissive outflow) using first-order Rusanov and second-order MUSCL schemes; a grid-convergence study and an exact mass-conservation audit confirm the numerics. Counterfactual simulations quantify ramp metering, an acceleration lane, and merge capacity drop, and identify merge friction as the dominant lever near capacity.

Validation and future work Against independent mainline observations the model reproduces the diurnal timing of congestion ($r = 0.88$) but under-predicts its amplitude ($R^2 = 0.34$). A boundary-only diagnostic (Section 5.2) localizes the cause: Calibrating the upstream inflow narrows the gap ($R^2 \to 0.46$) but cannot close it, because the observed afternoon density sits on the congested branch, which the transmissive downstream boundary cannot produce at an interior station without a downstream bottleneck. Two prioritized extensions follow: (i) add a downstream boundary/bottleneck condition (a prescribed downstream capacity or congested outflow state, e.g., representing the Makkah

Road interchange) so the model can reach congested-branch densities at interior stations; and (ii) calibrate the upstream inflow to mainline data and validate at multiple stations. Until then the reported scenario percentages are simulated, not field-confirmed. The jam density is taken per lane with the corridor aggregated to a single macroscopic link; the single-ramp focus extends directly to the multi-ramp source; and a second-order (ARZ/PW) treatment would capture non-equilibrium merge dynamics beyond the capacity-factor emulation used here.

Code and data availability

The simulation code and the calibration and validation datasets are openly available at `https://github.com/abdulazizalsamil-web/KFR.Traffic_model1.-.git`.

Author contributions

Yasser Almoteri and Abdulaziz Alsamil jointly share the conceptualization, formal analysis, and investigation of this study. Almoteri was responsible for the mathematical modeling, including the ODE–PDE coupling. Alsamil designed and implemented the finite-volume numerical scheme with CFL and grid-convergence analyses, non-dimensionalization, well-posedness analysis, curated the traffic data, managed project administration, developed the simulation software, validated the model against independent mainline observations, produced all figures, and drafted the numerical methods, results, and policy discussion. Both authors reviewed and edited the final manuscript. All authors have read and approved the final version of the manuscript for publication.

Use of Generative-AI tools declaration

The authors declare they have not used Artificial Intelligence (AI) tools in the creation of this article.

Acknowledgments

This work was supported and funded by the Deanship of Scientific Research at Imam Mohammad Ibn Saud Islamic University (IMSIU) (grant number IMSIU-DDRSP2602).

Conflict of interest

The authors declare no conflict of interest.

References

1. M. Alkhresheh, *Urban sprawl in Riyadh: Assessing the impacts of horizontal expansion on sustainability and quality of life. In URBAN INNOVATION: TO BOLDLY GO WHERE NO CITIES HAVE GONE BEFORE. Medium sized cities and towns as a major arena of global urbanisation*, Proceedings of REAL CORP 2025, 30th Intl. Conference on Urban Development, Regional Planning and Information Society (pp. 973-980). CORP–Competence Center of Urban and Regional Planning. 2025. Available from: `http://repository.corp.at/id/eprint/1194`.

2. N. M. Alshabibi, Impact assessment of integrating AVs in optimizing urban traffic operations for sustainable transportation planning in Riyadh, *World Electr. Vehic. J.,* **16** (2025), 246. https://doi.org/10.3390/wevj16050246

3. E. G. A. Osman, H. Y. A. Mohammed, A mathematical model for assessing the economic and social impacts of traffic congestion an applied study on Riyadh city, *J. Cult. Anal. Soc. Change*, 2025, 1022–1044. https://doi.org/10.64753/jcasc.v10i4.2971

4. Z. E. A. Kherroubi, S. Aknine, Review of driver behaviour modelling for highway on-ramp merging, *IET Intell. Transp. Sy.,* **18** (2024), 2793–2813. https://doi.org/10.1049/itr2.12572

5. D. Z. Mitkas, I. Politis, Evaluation of alternative Ramp Metering scenarios on freeway on-ramp with the use of microscopic simulation software Vissim, *Transp. Res. Proc.,* **45** (2020), 483–490. https://doi.org/10.1016/j.trpro.2020.03.042

6. P. Cazorla, F. Calderón, E. Avila-Ordóñez, Ramp metering strategies: A literature review, *Rev. Politécnica,* **50** (2022), 15–26. https://doi.org/10.33333/rp.vol50n1.02

7. S. Trubia, S. Curto, S. Barberi, A. Severino, F. Arena, G. Pau, Analysis and evaluation of ramp metering: From historical evolution to the application of new algorithms and engineering principles, *Sustainability,* **13** (2021), 850. https://doi.org/10.3390/su13020850

8. T. Alexakis, N. Peppes, E. Adamopoulou, K. Demestichas, An artificial intelligence-based approach for the controlled access ramp metering problem, *Vehicles,* **3** (2021), 63–83. https://doi.org/10.3390/vehicles3010005

9. C. Zhang, W. Ma, J. Zhao, C. Ma, Y. Su, X. Yang, Destination-aware coordinated ramp metering for preventing off-ramp queue spillover and mainstream congestion, *IEEE Intel. Transp. Sy.,* **16** (2023), 40–61. https://doi.org/10.1109/MITS.2023.3323029

10. Y. Yang, S. Wang, Z. Li, A linear model predictive control-based ramp metering strategy for traffic flow analysis in continuous multi-bottleneck highway segments, *IET Intell. Transp. Sy.,* **19** (2025), e70113. https://doi.org/10.1049/itr2.70113

11. Z. Liu, Y. Wu, S. Cao, L. Zhu, G. Shen, A ramp metering method based on congestion status in the urban freeway, *IEEE Access,* **8** (2020), 76823–76831. https://doi.org/10.1109/ACCESS.2020.2990646

12. J. Wei, K. Long, J. Gu, Z. Zhou, S. Li, Freeway ramp metering based on PSO-PID control, *PLoS One,* **16** (2021), e0260977. https://doi.org/10.1371/journal.pone.0260977

13. J. Cheng, C. Ye, N. Wang, Y. Yao, H. Zhao, X. Dai, et al., A deep reinforcement learning based ramp metering control method considering ramp outflow, *IFAC-PapersOnLine,* **58** (2024), 200–205. https://doi.org/10.1016/j.ifacol.2024.07.340

14. N. Sacchi, M. Cucuzzella, A. Ferrara, Constrained ramp metering control based on sliding mode unknown input observers, *Eur. J. Control,* 2025, 101329. https://doi.org/10.1016/j.ejcon.2025.101329

15. H. H. S. N. Subraveti, V. L. Knoop, B. Van Arem, Lane change control combined with ramp metering: A strategy to manage delays at on-ramp merging sections, *J. Adv. Trans.,* **2021** (2021), 8638523. https://doi.org/10.1155/2021/8638523

16. C. Liu, Z. Wang, Ramp metering influence on freeway operational safety near on-ramp exits, *Int. J. Trans. Sci. Tech.,* **2** (2013), 87–94. https://doi.org/10.1260/2046-0430.2.2.87

17. H. J. Haule, M. S. Ali, P. Alluri, T. Sando, Evaluating the effect of ramp metering on freeway safety using real-time traffic data, *Accident Anal. Prev.,* **157** (2021), 106181. https://doi.org/10.1016/j.aap.2021.106181

18. H. J. Haule, P. Alluri, T. Sando, A. Gan, Analyzing the effectiveness of ramp metering in alleviating crash-related congestion on freeways, *Transport. Plan. Tech.,* **46** (2023), 599–614. https://doi.org/10.1080/03081060.2023.2203694

19. X. Ma, A. Karimpour, Y. J. Wu, Data-driven transfer learning framework for estimating on-ramp and off-ramp traffic flows, *J. Intell. Trans. Syst.,* **29** (2025), 67–80. https://doi.org/10.1080/15472450.2023.2301696

20. A. Nohekhan, S. Zahedian, A. Haghani, A deep learning model for off-ramp hourly traffic volume estimation, *Transport. Res. Rec.,* **2675** (2021), 350–362. https://doi.org/10.1177/03611981211027151

21. J. Chen, L. Lin, R. Jiang, Assigning on-ramp flows to maximize capacity of highway with two on-ramps and one off-ramp in between, *Physica A,* **465** (2017), 347–357. https://doi.org/10.1016/j.physa.2016.08.053

22. X. Zhang, Y. Han, Multi-Agent reinforcement learning for traffic state estimation on highways using fundamental diagram and LWR theory, *Appl. Sci.,* **16** (2026), 1219. https://doi.org/10.3390/app16031219

23. M. Malekzadeh, I. Papamichail, M. Papageorgiou, K. Bogenberger, Ramp metering for lane-free traffic of automated vehicles via ramp vehicle speed control, *Transport. Res. C-Emer.,* **179** (2025), 105302. https://doi.org/10.1016/j.trc.2025.105302

24. Y. Zhou, J. Chen, E. Chung, K. Ozbay, CAV-enabled active resolving of temporary mainline congestion caused by gap creation for on-ramp merging vehicles, *IEEE T. Intell. Transp.,* **25** (2023), 6873–6888. https://doi.org/10.1109/TITS.2023.3340170

25. M. Liu, Y. Zhao, J. Wang, L. Li, H. Tan, *A DRL-based multi-modal local congestion index method for mixed on-ramp merging*, Intelligent Transportation Engineering: Proceedings of the 9th International Conference (ICITE 2024), 2025, 434–445. https://doi.org/10.3233/ATDE250443

26. H. Yu, L. Zhang, M. Zhang, F. Jin, Y. Wang, Coordinated ramp metering considering the dynamics of mixed-autonomy traffic, *Sustainability,* **16** (2024), 10055. Available from: `https://www.mdpi.com/2071-1050/16/22/10055`.

27. F. A. Chiarello, *An overview of non-local traffic flow models*, Mathematical descriptions of traffic flow: micro, macro and kinetic models, 2020, 79–91. https://doi.org/10.1007/978-3-030-66560-9

28. M. L. Delle Monache, S. Samaranayake, J. Reilly, W. Krichene, P. Goatin, A. Bayen, A PDE-ODE model for a junction with ramp buffer, *SIAM J. Appl. Math.,* **74** (2014), 22–39. https://doi.org/10.1137/130908993

29. O. Kolb, S. Göttlich, P. Goatin, Capacity drop and traffic control for a second order traffic model, *Netw. Heterog. Media,* **12** (2017), 663–681. https://doi.org/10.3934/nhm.2017027

30. N. Kolbe, M. Berghaus, E. Kalló, M. Herty, M. Oeser, A microscopic on-ramp model based on macroscopic network flows, *Appl. Sci.,* **14** (2024), 9111. https://doi.org/10.3390/app14199111
31. T. Q. Tang, H. J. Huang, S. C. Wong, Z. Y. Gao, Y. Zhang, A new macro model for traffic flow on a highway with ramps and numerical tests, *Commun. Theor. Phys.,* **51** (2009), 71–78. https://doi.org/10.1088/0253-6102/51/1/15
32. L. Xu, J. Lu, Y. Zheng, K. He, S. Zhang, Study on mixed traffic characteristics around highway on-ramp bottleneck using a microscopic simulation model, *Physica A,* **654** (2024), 130134. https://doi.org/10.1016/j.physa.2024.130134
33. H. Ru, J. Luan, Q. Ding, J. Xu, Influence of traffic flow of on-ramps on the mainline speed on freeways, *Arch. Trans.,* **69** (2024), 59–73. https://doi.org/10.61089/aot2024.b2h1zb09
34. A. Srivastava, N. Geroliminis, Empirical observations of capacity drop in freeway merges with ramp control and integration in a first-order model, *Transport. Res. Part C-Emer.,* **30** (2013), 161–177. https://doi.org/10.1016/j.trc.2013.02.006